Journal of
Composites Science

MDPI

Article

Use of Zr–Ti Alloy Melt Infiltration for Fabricating Carbon-Fiber-Reinforced Ultrahigh-Temperature Ceramic Matrix Composites

Yutaro Arai [1], Tomoki Marumo [2] and Ryo Inoue [2,*]

[1] Department of Materials Science and Technology, Tokyo University of Science, 6-3-1 Niijyuku, Katsushika-ku, Tokyo 125-8585, Japan; arai.yutaro@rs.tus.ac.jp
[2] Department of Mechanical Engineering, Tokyo University of Science, 6-3-1 Niijyuku, Katsushika-ku, Tokyo 125-8585, Japan; 4521557@ed.tus.ac.jp
* Correspondence: inoue.ryo@rs.tus.ac.jp; Tel.: +81-3-5876-1321

Abstract: Carbon-fiber-reinforced ultrahigh-temperature ceramic (C/UHTC) matrix composites are an attractive candidate for fabricating various hot structures. The present study aimed to establish a Si-free Zr–Ti melt-infiltration method for fabricating C/UHTC matrix composites. To achieve this, the wettability of Zr–Ti alloys on carbon and their reactivity to carbon were examined. The alloys were melted on graphite plates and infiltrated into model preforms, which were made of porous carbon and had median pore diameters of 3 μm. The results showed that the apparent contact angle between Zr–Ti and C measured from melted alloys on carbon in room temperature was ~20–42° and that the alloys infiltrated into the preforms regardless of the Zr or Ti content. However, with an increase in the Zr content in the alloys, carbon disappeared and was absorbed into the alloys since the reactivity of Zr was higher than that of Ti and the specific surface area of the porous preform was higher than that of carbon-fiber-reinforced carbon composites, which are a typical preform of C/UHTC matrix composites. These results clearly indicate that not only the capillary flow during infiltration but also the reactivity of alloys to preforms should be considered in the process design for fabricating high-density composites via Zr–Ti infiltration.

Keywords: melt infiltration; Zr–Ti alloys; ultrahigh-temperature ceramic composites; capillary flow

Citation: Arai, Y.; Marumo, T.; Inoue, R. Use of Zr–Ti Alloy Melt Infiltration for Fabricating Carbon-Fiber-Reinforced Ultrahigh-Temperature Ceramic Matrix Composites. *J. Compos. Sci.* **2021**, *5*, 186. https://doi.org/10.3390/jcs5070186

Academic Editor: Gérard L. Vignoles

Received: 25 June 2021
Accepted: 15 July 2021
Published: 16 July 2021

1. Introduction

Transition metal borides and carbides with melting temperatures of >2500 °C are well known as ultrahigh-temperature ceramics (UHTCs) [1–3]. Some Ti-, Zr-, and Hf-based UHTCs and their composites with a dispersed second phase, such as SiC, $MoSi_2$, and $ZrSi_2$ can be used in oxidizing atmospheres due to the fact that an oxide scale is formed, which prevents further oxidation [4–7]. Moreover, the fracture toughness of UHTCs is almost the same as that of conventional engineering ceramics (2–6 $MPa\sqrt{m}$) [2], and the density of UHTCs is relatively high (~6 g/cm^3 or higher) [1–3]. To facilitate the use of UHTCs in fabricating hot structures, such as leading edges and nose cones for hypersonic vehicles and thermal protection systems for re-entry vehicles, carbon-fiber-reinforced UHTC (C/UHTC) matrix composites have been developed [8]. C/UHTC matrix composites are classified as ceramic matrix composites (CMCs) and have good damage tolerance since carbon fibers prevent unstable crack propagation even after matrix cracking occurs in UHTCs [9,10]. Since the oxidation behavior of C/UHTC matrix composites is similar to that of monolithic UHTCs, C/UHTC matrix composites are also considered as an attractive candidate for the hot structures mentioned above [8,11].

To process C/UHTC matrix composites, conventional fabrication methods used for CMCs such as sintering, chemical vapor infiltration (CVI), polymer impregnation and pyrolysis (PIP), and melt infiltration (MI) based on Si (Si-MI) have been employed. Sintering is a traditional technique used for dense polycrystalline ceramics. However, it is difficult to manufacture components that are large or have complicated shapes by this technique [12,13]. CVI and PIP are often used for the fabrication of UHTC composites [14–17]. However, CVI and PIP require repeated infiltration of organic compounds. Thus, these techniques have a longer process time (>10 cycles) than other techniques. Moreover, CVI and PIP require complex organic compounds for the formation of UHTC matrices.

MI methods based on Si and Si alloys (e.g., Si–Hf, Si–Ti, Si–Zr) have a shorter process time than CVI and PIP since melted Si can easily infiltrate preforms containing carbon-based UHTC powders and react to form a SiC matrix [18–21]. Generally, the MI process has been used for fabricating C/SiC composites, which are used as wear components [22–24]. In the case of C/UHTC composites, melted Si also reacts with preforms containing UHTC powders. However, the generation of reaction-formed products with lower melting temperatures than Si is inevitable. The authors fabricated C/ZrB_2–SiC–ZrC composites by Si and Si-$ZrSi_2$ eutectic with a melting temperature of ~1380 °C. However, severe degradation occurs during heat exposure at 1700 °C in air since the eutectic mixture melts and flows toward the outside of the composites under dynamic pressure [11,25]. Moreover, SiO(g) is formed by the oxidation of Si and/or SiC, which is not desirable for UHTC matrix composites exposed to temperatures above 2000 °C, since a SiO_2(l) layer, which is well known as a barrier to oxygen diffusion, is not formed on the surface by the oxidation of Si and/or SiC [26,27]. Since SiO(g) is a gaseous species, the oxidation of Si and/or SiC causes the formation of a porous layer and the oxidized region is delaminated from the porous region [3,4,28,29]. Thus, the development of a Si-free MI method is required for the formation of C/UHTC matrix composites.

MI metals (or alloys) and their melting points are summarized in Figure 1. As a Si-free MI process, Zr-based MI (Zr-MI) has been applied to the formation of C/ZrC composites [30]. Zr is successfully infiltrated into the carbon preform, and ZrC is formed as a matrix. Zr-MI is one of the solutions to fabricate Si-free composites. However, a process temperature of ~2000 °C is required since the melting point of Zr is very high (~1875 °C). To reduce the process temperature of Zr-MI, this study focuses on Zr–Ti alloy MI into porous carbon preforms. The minimum melting point of the Zr–Ti alloy is ~1540 °C (Ti-37at%Zr) and is similar to the melting point of Si [31]. In addition, ZrC and TiC, which are formed by the reaction of Zr and Ti with C, respectively, have high melting points and are classified as UHTCs.

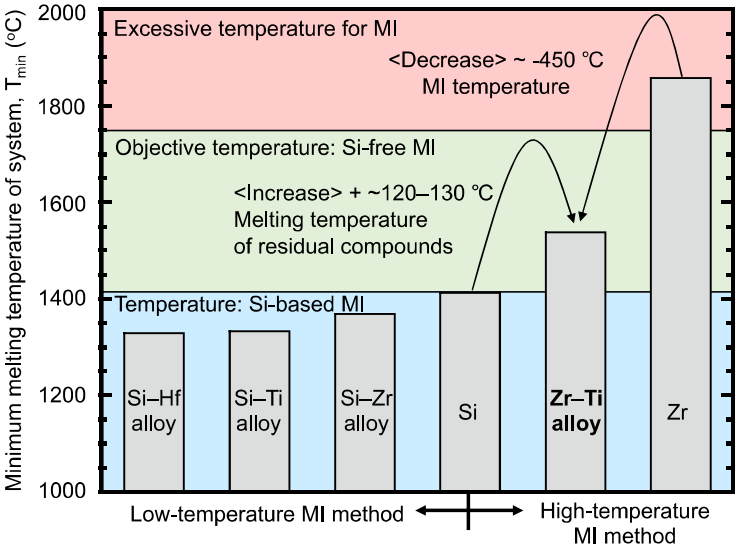

Figure 1. Temperature required for melt infiltration (MI) of various metals and alloys.

Thus, Zr–Ti MI is an attractive solution for the development of lightweight C/UHTC matrix composites. In the case of the Zr–Ti MI process, microstructural control is important. However, the control is difficult to achieve since physical phenomena such as capillary formation between carbon and the liquid alloy, interfacial reactions, and permeability of the liquid alloy during infiltration are still not well understood. These phenomena are dependent on infiltration conditions such as the temperature, time, and the porous structure of preforms as well as the physical properties of alloys. To the best of the authors' knowledge, the relationship among capillary flow, reactivity, and infiltration behavior is still not known.

Thus, the objective of this study is to provide fundamental experimental data for the infiltration of Zr–Ti into porous media and thereby to facilitate the application of the Zr–Ti MI process to the fabrication of novel lightweight C/UHTC matrix composites. In the present study, the effect of the composition of Zr–Ti alloys on interfacial reactions and the permeability of the alloys to model porous carbon preforms are considered. The infiltration behavior and the microstructures and reaction-formed products after MI are discussed.

2. Materials and Methods

2.1. Preparation of Zr–Ti Alloys for MI

Zr and Ti chunks (99.9%, Kojundo Kagaku Co., Ltd., Saitama, Japan) were used as raw materials. Zr–Ti alloys were fabricated in an arc-melting furnace (Nissin Giken, Saitama, Japan). Arc-melting was carried out in Ar atmosphere and ingots with the diameter of ~70 mm and the thickness of ~10 mm were obtained. To ensure homogeneity of the alloys, arc melting was repeated four times. In the present study, Zr–Ti alloys with three different compositions were prepared; the alloys were Ti-12at%Zr (20wt%Zr), Ti-37at%Zr (52wt%Zr), and Ti-80at%Zr (88wt%Zr), which were denoted as TZ12, TZ37, and TZ80, respectively. For a Zr–Ti binary system, the melting temperatures of these alloys were ~1540–1750 °C, which are lower than that of Zr (Figure 2).

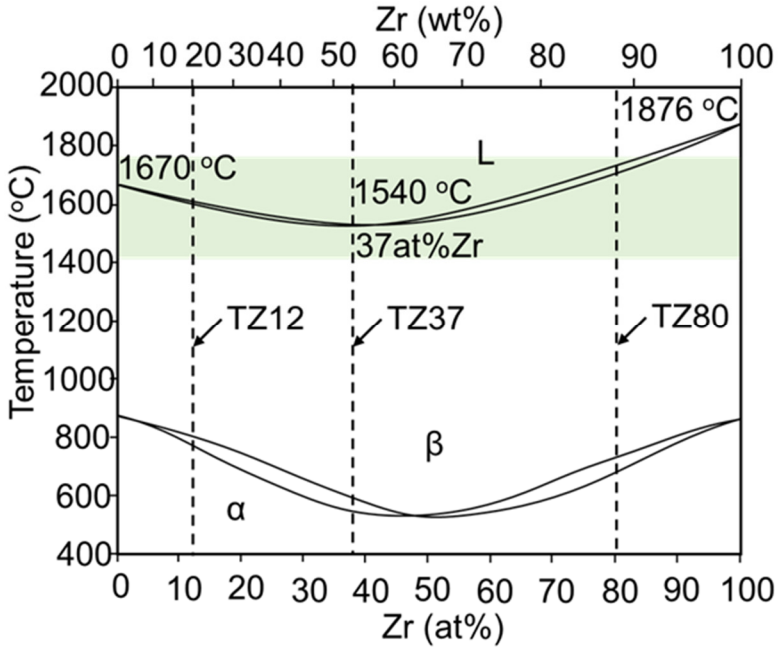

Figure 2. Phase diagram for Zr–Ti system.

2.2. Measurement of Wetting Angle between Graphite and Zr–Ti Alloy

To evaluate the wettability of Zr–Ti alloys on carbon, a graphite plate with dimensions of 25 mm × 25 mm × 5 mm (thickness) was prepared as a substrate with a roughness of less than 10 μm. Zr–Ti alloys with dimensions of 5 mm × 5 mm × 5 mm were cut from ingot and set on the graphite plate. Next, the plate with the alloys was set into a carbon furnace and heated at a rate of 50 °C/min. The alloys were melted at 1750 °C for 15 min in an Ar atmosphere. Since the melting point of alloys were ~1560–1700 °C, alloys existed as liquid for 17–23 min during exposure. To prevent oxidation, Ar was introduced into the furnace and the furnace chamber was vacuumized thrice before MI. Then, the furnace was cooled and the samples were removed from the furnace below 200 °C.

2.3. Infiltration of Zr–Ti Alloys into Porous Media

Porous carbon materials with continuous pore structures were used as model preforms. The median pore diameter was ~3 μm, which was measured by mercury porosimeter with the pressure of mercury by 0.024–414 MPa [32,33]. Details of the model preform microstructures have already been reported. The model material is composed of glassy carbon derived from the carbonization of a resole-type phenolic resin. In the present study, three Zr–Ti alloys with different compositions were melted and infiltrated into the model preforms with dimensions of 4 mm × 6 mm × 60 mm (thickness). The preforms with the alloys were set into graphite crucibles with a diameter of 10 mm and a depth of ~15 mm. To prevent a reaction between the crucibles and Zr–Ti alloys, the crucibles were coated with boron nitride (BN) by spraying (h-BN spray, Showa Denko Co., Ltd., Nagano, Japan). The Zr–Ti alloys (~2 g) were set into the coated crucibles, and porous carbons were placed on the Zr–Ti alloys vertically. Then, porous carbons were fixed with BN coated carbon fiber reinforced carbon composites (C/C) jig not to tilt during processing. Zr–Ti alloy MI was carried out under the same conditions described in the previous subsections. For comparison purposes, acetone was also infiltrated into porous carbon at room temperature (25 °C) in air to observe the infiltration behavior briefly. Acetone infiltration is a well-known method for confirming infiltration behavior in porous media [34].

2.4. Microstructural Characterization

After infiltration, the graphite plates and model preforms containing the Zr–Ti alloys were embedded in epoxy resin and cut into two pieces to measure the wetting angle between the Zr–Ti alloys and graphite and to understand the reaction between them through cross-sectional observation. The embedded specimens were also cut and polished using diamond paste up to a depth of 1 μm. The specimen microstructures were observed by scanning electron microscopy (SEM, S-3000H, TM-3000, Hitachi High-Tech Corporation, Tokyo, Japan), and elemental analysis was carried out by energy-dispersive X-ray spectroscopy (EDX, oxford Instruments, Aztec micsF+ x-stream-2, Abingdon, UK). To evaluate the crystal structures of the specimens, powder X-ray diffraction (XRD, MiniFlex600, Rigaku Corporation, Tokyo, Japan) analysis was carried out. The X-ray wavelength, scan speed, and diffraction angle range were 0.154 nm (CuKα), 2°/min, and 20–80°, respectively.

3. Results and Discussion

3.1. Wetting between Graphite and Zr–Ti Alloys

The typical cross sections of the melted Zr–Ti alloys on the graphite plate are shown in Figure 3. For all the compositions, the Zr–Ti alloys melted and spread on the graphite plate. The spread length seemed to increase with an increase in the Zr content in the alloys. The apparent contact angle (φ), which is defined as shown in Figure 3, for TZ12, TZ37, and TZ80 was 20°, 41°, and 42°, respectively. Since the angle is measured from melted alloys on graphite plate at room temperature, it is defined as the "apparent" contact angle.

The angle increased with a decrease in the Ti content in the Zr–Ti alloys. Since the coefficient of thermal expansion (CTE) of C (~0–0.1 × 10^{-6}/°C) is considerably lower than that of the alloys (~6–8 × 10^{-6}/°C) and carbides (~7–9 × 10^{-6}/°C), tensile stress is induced by CTE mismatch and causes partial delamination, which does not affect the apparent contact angle of the spread alloys since delamination occurs during cooling. The interfacial reaction between carbon and the alloys during processing is discussed in detail in Section 3.3.

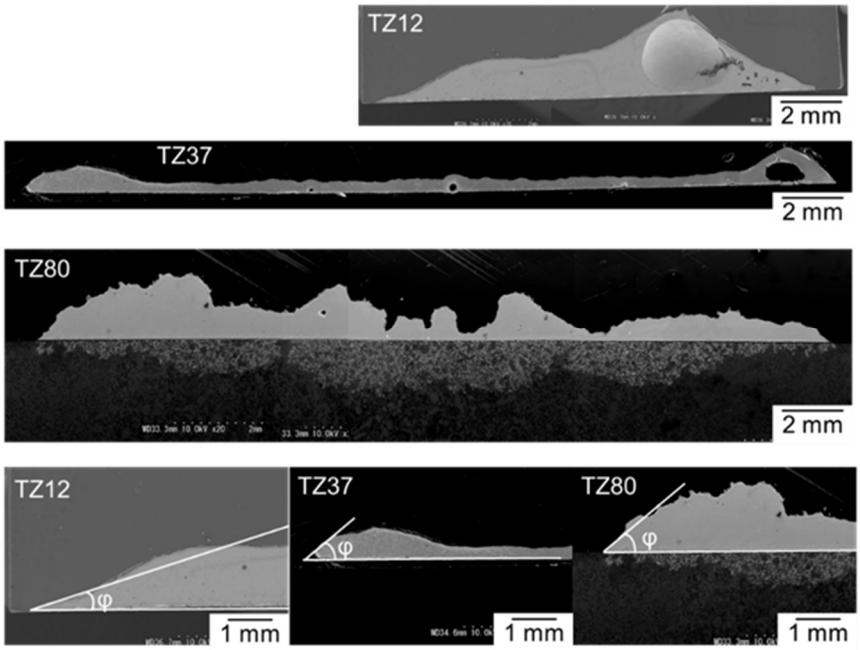

Figure 3. Macroscopic scanning electron microscopy (SEM) images of melted alloys on graphite plate. The apparent contact angles of the alloys are also defined.

3.2. Infiltration of Zr–Ti Alloys into Model Preform

The typical microstructures of the model preform after infiltration are shown in Figure 4. The alloys infiltrate from the bottom to the top. Hence, the infiltration height is defined as the distance between the bottom of the model preform and the top of the infiltrating alloys (Figure 4).

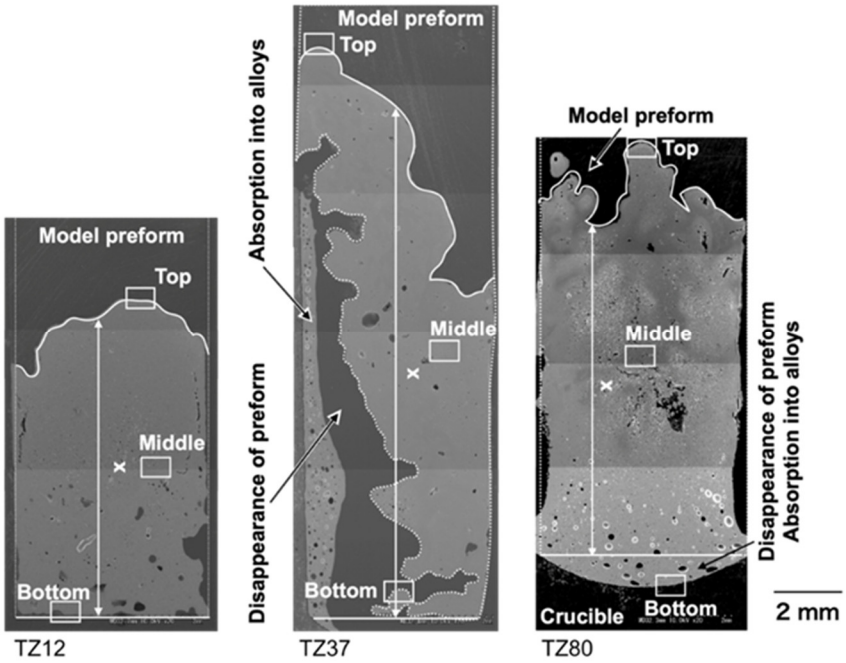

Figure 4. Macroscopic SEM images of infiltrated model preforms. Here, "×" represents the infiltration height.

The relationship between the infiltration height x and time t is shown in Figure 5. The estimated curves are expressed by Washburn's equation [34] as follows:

$$x = \sqrt{\frac{\gamma \cos \varphi}{2\mu} rt}, \quad (1)$$

where γ, φ, μ, and r represent the surface tension, wetting angle, fluid viscosity, and pore radius of the media, respectively. Moreover, assuming that the entire amount of the alloy infiltrates into porous carbon, the ideal infiltrated distance (height) x_{ideal} can be calculated by using the alloy volume V_{alloy} and the cross-sectional area S of porous carbon as follows:

$$x_{ideal} = \frac{V_{alloy}}{S}. \quad (2)$$

Since the density of the Zr–Ti alloy is between the densities of Ti (4.51 g/cm^3) and Zr (6.52 g/cm^3) even when the Zr and Ti content in the alloys varies according to the reaction, it is recognized that 13–18 mm is the ideal height of the infiltrating alloy under the present conditions.

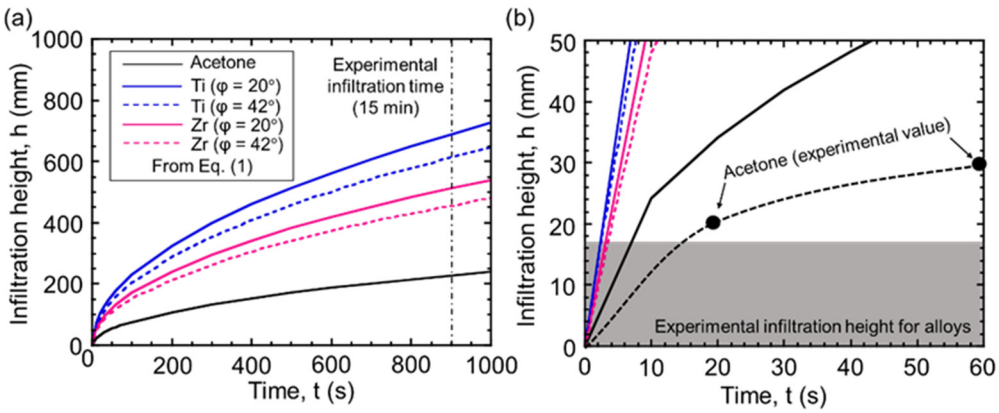

Figure 5. (**a**) Relationship between calculated infiltration height and time. (**b**) Enlarged view of (**a**) along with experimental values.

The infiltration height for acetone was ~20 mm at 20 s and ~30 mm at 60 s. After 600 s, acetone was fully infiltrated. In addition, the infiltration heights for TZ12, TZ37, and TZ80 were 8.9 ± 0.8, 14 ± 3.5, and 11 ± 1.6 mm, respectively. The infiltration terminated within a few seconds for all the alloys. These results and estimations clearly reveal that the infiltration of the Zr–Ti alloy into the model preform depends on not only the capillary flow but also the reactivity among Zr, Ti, and C.

3.3. Microstructures of Model Materials

The results of a detailed observation of the interface between the melted alloys and graphite plate along with the results of EDX point analysis are shown in Figure 6. Backscattered electron (BSE) images clearly showed two contrasting regions: a brighter gray contrast region and a darker gray contrast region. The uniform darker gray contrast region was observed in the outside regions of TZ12 and TZ37. In the inside regions of TZ12 and TZ37, the two contrast regions were mixed. However, TZ80 had a uniform brighter gray contrast region. Since, the contrast in BSE images is determined by the atomic number, a bright contrast indicates a Zr-rich phase and a dark contrast indicates a Ti-rich phase. Although the content of elements obtained by EDX is qualitative, EDX point analysis confirmed that the Zr content in the inside region (Point B) was greater than the Ti content in the outside region (Point A). Notably, C was detected at both Points A and B.

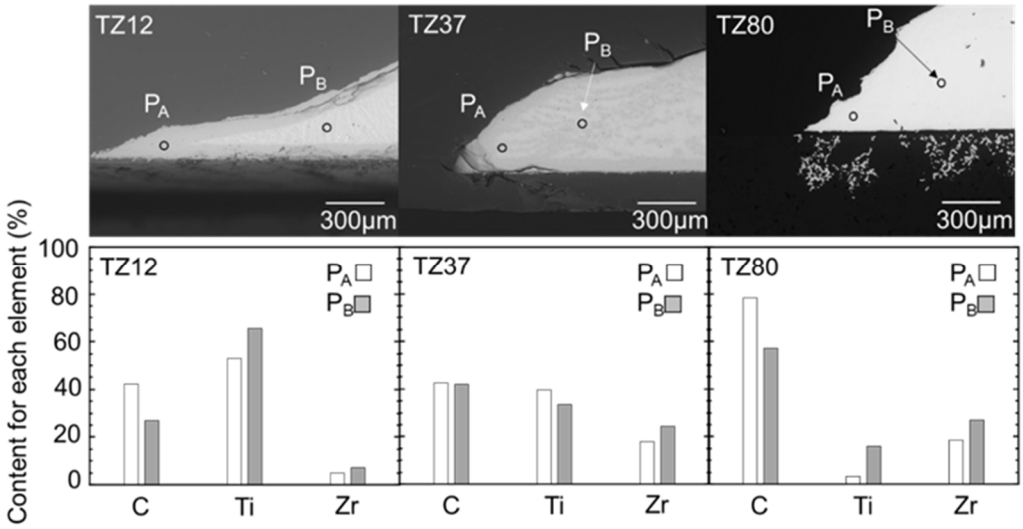

Figure 6. Enlarged backscattered electron (BSE) images of melted alloys on graphite plate along with results of energy-dispersive X-ray (EDX) point analysis for C, Ti, and Zr.

The enlarged views of the top, middle, and bottom regions of the infiltrated model preform are shown in Figure 7. Each of these regions is defined in Figure 4. Although the brightness and distribution of contrast were different, the darker and brighter contrast regions (Points D and B in Figure 7) were mixed in the middle and bottom regions of the specimen. In all the model preforms, the top region exhibited uniform contrast.

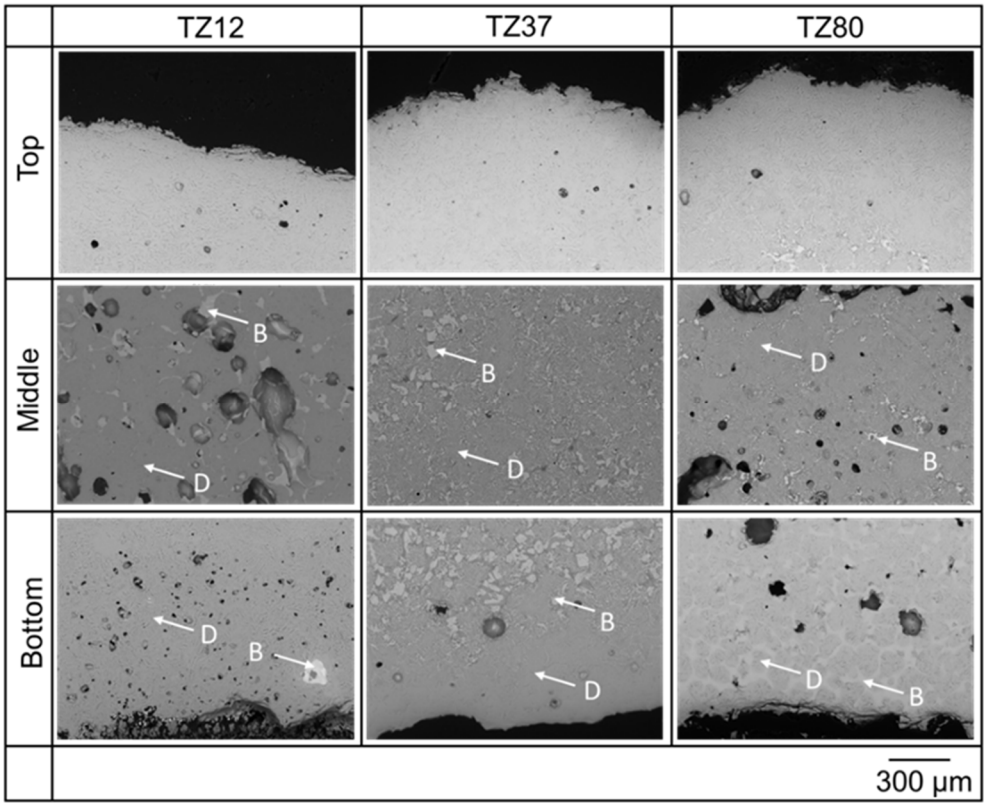

Figure 7. Enlarged BSE images obtained after infiltration into model preforms. The areas considered in Figure 7 are marked in Figure 4. Points B and D show brighter gray contrast and darker gray contrast, respectively.

The XRD patterns in Figure 8a indicate that the diffraction peaks of the model preforms are located between those of TiC and ZrC [35,36] for each plane index. This means that there exist patterns for $Zr_xTi_{1-x}C$ with a NaCl structure, which is the same structure as those for TiC and ZrC. There are no patterns for residual alloys, which is a reasonable observation since ZrC and TiC are both proportional solid solution compounds and the alloys are fully converted to carbides. Peaks of carbons are also not detected due to the fact that the model preform is composed of glassy carbon. By focusing on the lattce parameter a of $Zr_xTi_{1-x}C$, the Zr and Ti concentrations in $Zr_xTi_{1-x}C$ were evaluated from the XRD patterns, as shown in Figure 8b [37]. The (111) peaks of $Zr_xTi_{1-x}C$ at 2θ = 33.54–35.64° (33.54°, 33.58°, 34.82°, and 35.64°) can be observed in Figure 8a. Based on Bragg's law, the diffraction condition, which is well known, can be expressed in terms of the lattice spacing d, diffraction angle θ, and X-ray wavelength λ (λ = 0.154 nm for a CuKα radiation source) as follows:

$$2d \sin\theta = \lambda. \quad (3)$$

The crystal structure of $Zr_xTi_{1-x}C$ is cubic. The relationship between the lattice parameter and lattice spacing is expressed as follows:

$$a = d\sqrt{h^2 + k^2 + l^2}, \quad (4)$$

where h, k, and l represent the plane indices. From Equations (3) and (4), the lattice parameters corresponding to the (111) peaks with 2θ = 33.54°, 33.58°, 34.82°, and 35.64° are 0.4622, 0.4617, 0.4457, and 0.4358 nm, respectively. Therefore, these results imply that $Zr_xTi_{1-x}C$ (x = 0.05–0.73) is formed. TZ80 forms Zr-rich carbides, whereas TZ12 forms Ti-rich carbides. In contrast, TZ37 forms carbides with Zr-rich, Ti-rich, and intermediate compositions.

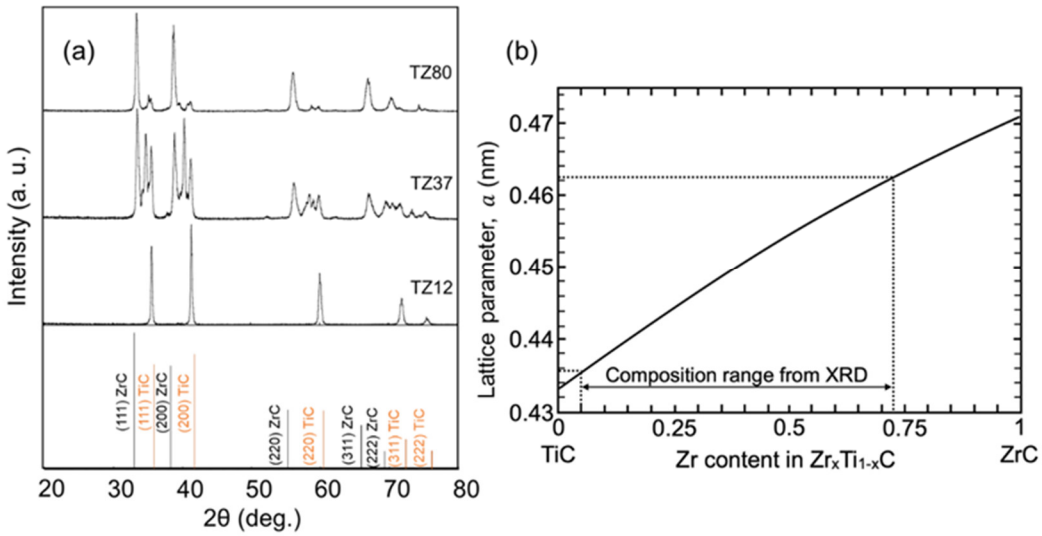

Figure 8. (**a**) Powder X-ray diffraction (XRD) patterns obtained after infiltration into model preforms. (**b**) Relationship between lattice parameter and Zr content in $Zr_xTi_{1-x}C$.

To explain microstructural differences, a pseudobinary phase diagram was obtained for the TiC–ZrC system, as shown in Figure 9 [38]. The diagram clearly shows that spinodal and binodal decomposition occurs in the system depending on the composition of TiC and ZrC. Thus, a uniform distribution of darker and brighter contrast regions is formed by spinodal decomposition (TZ37 and TZ80), and separate darker and brighter contrast regions are formed by binodal decomposition (TZ12). The uniform contrast region in the top and bottom regions is considered to represent the phases where the Ti content is considerably greater than the Zr content since it is difficult for spinodal or binodal decomposition to occur in Ti-rich $Zr_xTi_{1-x}C$ (x = 0.05 or less) owing to the fact that $Zr_xTi_{1-x}C$ contains Zr in the range of 5–73 at%.

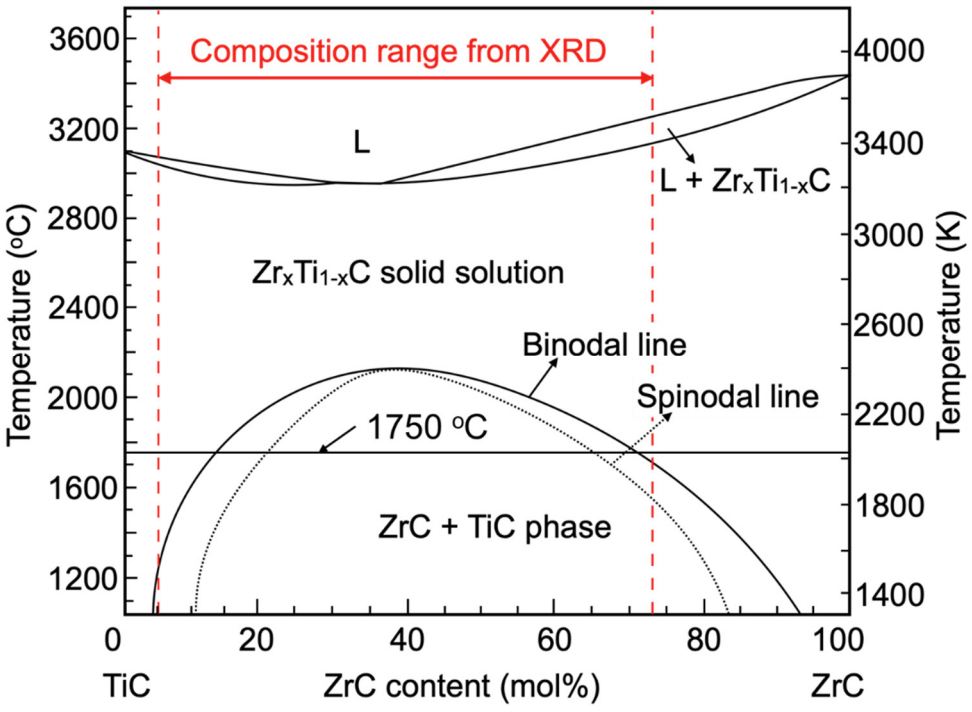

Figure 9. Pseudobinary phase diagram for TiC–ZrC system.

To investigate the reactivity between the alloys and carbon, the Gibbs free energy of formation (ΔG_f) for TiC and ZrC [39] was determined, as shown in Figure 10. For TiC and ZrC, the ΔG_f values at 1750 °C were −158 and −180 kJ/mol, respectively. This implies that the formation of ZrC is more stable than that of TiC thermodynamically. Hence, the melting points of TZ12 and TZ80 vary during infiltration, and as infiltration progresses, further infiltration becomes difficult since the Ti content in the alloys causes an increase (TZ12) or decrease (TZ80) in the melting point (Figure 2). In addition, the flow of TZ37 and TZ80 on the graphite plate probably continues after the formation of carbides at the alloy–graphite interface.

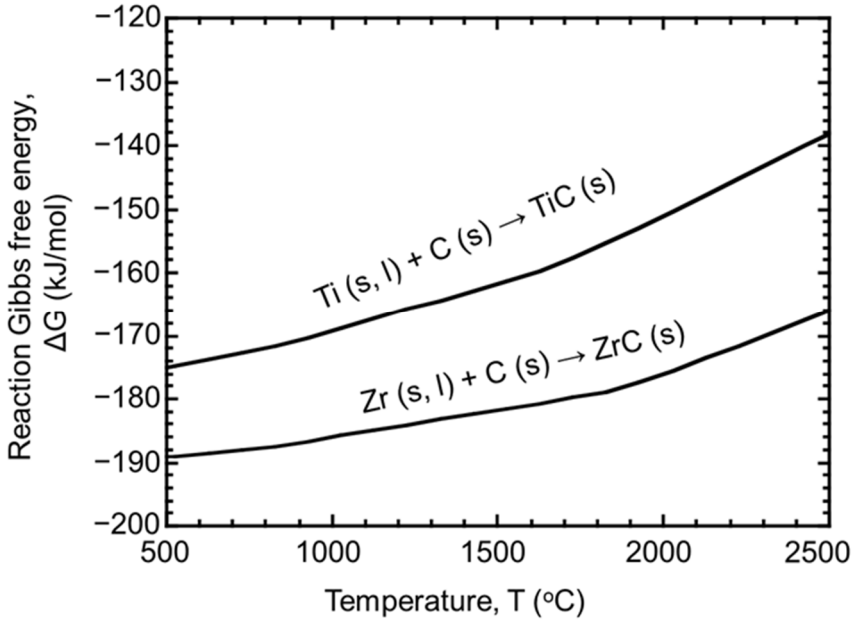

Figure 10. Gibbs free energy of formation for TiC and ZrC.

During the infiltration of the alloys into the model preforms, carbons are diffused into the alloys to form carbides since the solid solubility limit of C for Ti and Zr is only ~1 at%. Then, the disappearance and absorption of carbon (mentioned in Section 3.2) are mainly induced by the reaction between Zr and C. This phenomenon is accelerated by the large specific surface area of the model preform (2.23 m^2/g). To consider the fabrication of C/UHTC matrix composites by Zr–Ti alloy MI, C/C composites are used as the preform. Generally, the size of the transverse cracks in C/C composites, which are considered as channels during infiltration, is 10–20 μm, which is considerably higher than that of the porous carbons used in this study. This implies that the disappearance and absorption of carbon are not as critical as those of the model preform for the fabrication of C/UHTC matrix composites since the specific surface area of the transverse cracks is ~0.03 m^2/g, which is considerably smaller than that of the model preform. These results indicate that the infiltration condition for Zr–Ti alloys should be designed by considering not only the capillary flow but also the reactivity between the alloys and carbon. For the infiltration of C/C composites, TZ37 is the most suitable alloy since its melting point does not vary according to the reaction during infiltration as mentioned above, and hence, the design of the infiltration condition is easy.

4. Conclusions

To provide fundamental knowledge required for the development of novel C/UHTC composites by Zr–Ti alloy MI, the wetting behavior of Zr–Ti alloys on graphite and the infiltration of alloys into porous carbons were investigated. The conclusions obtained in the present study are summarized below.

The wetting of Zr–Ti alloys on carbon is favorable since the alloys are spread on the graphite plate and the wetting angles estimated from solidified samples are 20–42°. The spread length of TZ12 is smaller than those of TZ37 and TZ80. This is attributed to the increase in the melting point of TZ12 during melting since the reactivity of Zr and C is higher than that of Ti and C.

Zr–Ti alloys infiltrate into the model preforms regardless of the differences in composition. However, a part of the model preform disappears, and the disappearing part becomes larger as the Zr content in the alloys increases on account of the higher reactivity of Zr. This result clearly confirms that the design of Zr–Ti MI should consider not only the capillary flow but also the reactivity to the preform used for infiltration. For developing novel C/UHTC composites by the infiltration of alloys into C/C composites, TZ37 is the most suitable alloy since the melting point does not change owing to the reaction during infiltration. In addition, the disappearance and absorption of carbons are not as critical as those of the model preforms since the channels and specific surface area of C/C composites (~10–20 μm and ~0.03 m^2/g) are larger and smaller than those of the model preforms (~3 μm and ~2.23 m^2/g), respectively.

Author Contributions: Conceptualization, R.I. and Y.A.; methodology, Y.A.; validation, R.I., Y.A., and T.M.; formal analysis, Y.A.; investigation, Y.A. and T.M.; resources, R.I.; data curation, R.I. and Y.A.; writing—original draft preparation, Y.A.; writing—review and editing, R.I.; visualization, R.I.; supervision, R.I.; project administration, R.I. All authors have read and agreed to the published version of the manuscript.

Funding: This research was supported by JSPS KAKENHI Grant Number 21H01218.

Conflicts of Interest: The authors declare no conflicts of interest.

References

1. Fahrenholtz, W.G.; Hilmas, G.E.; Talmy, I.G.; Zaykoski, J.A. Refractory diborides of zirconium and hafnium. *J. Am. Ceram. Soc.* **2007**, *90*, 1347–1364, doi:10.1111/j.1551-2916.2007.01583.x.
2. Guo, S.-Q. Densification of ZrB_2–based composites and their mechanical and physical properties: A review. *J. Eur. Ceram. Soc.* **2009**, *29*, 995–1011, doi:10.1016/j.jeurceramsoc.2008.11.008.
3. Inoue, R.; Arai, Y.; Kubota, Y.; Kogo, Y.; Goto, K. Oxidation of ZrB_2 and its composites: A review. *J. Mater. Sci.* **2018**, 1–22, doi:10.1007/s10853-018-2601-0.
4. Fahrenholtz, W.G. Thermodynamic analysis of ZrB_2–SiC oxidation: Formation of a SiC-depleted region. *J. Am. Ceram. Soc.* **2007**, *90*, 143–148, doi:10.1111/j.1551-2916.2006.01329.x.
5. Silvestroni, L.; Meriggi, G.; Sciti, D. Oxidation behavior of ZrB_2 composites doped with various transition metal silicides. *Corros. Sci.* **2014**, *83*, 281–291, doi:10.1016/j.corsci.2014.02.026.
6. Lavrenko, V.A.; Panasyuk, A.D.; Protsenko, T.G.; Dyatel, V.P.; Lugovskaya, E.S.; Egorova, E.I. High-temperature reactions of materials of the ZrB_2–$ZrSi_2$ system with oxygen. *Sov. Powder Metall. Met. Ceram.* **1982**, *21*, 471–473, doi:10.1007/BF00801757.
7. Sciti, D.; Brach, M.; Bellosi, A. Oxidation behavior of a pressureless sintered ZrB_2–$MoSi_2$ ceramic composite. *J. Mater. Res.* **2005**, *20*, 922–930, doi:10.1557/JMR.2005.0111.
8. Glass, D.E. Ceramic matrix composite (CMC) thermal protection systems (TPS) and hot structures for hypersonic vehicles. In Proceedings of the 15th AIAA International Space Planes and Hypersonic Systems and Technologies Conference, Dayton, OH, USA, 28 April–1 May 2008; pp. 1–36.
9. Budiansky, B.; Hutchinson, J.W.; Evans, A.G. Matrix fracture in fiber-reinforced ceramics. *J. Mech. Phys. Solids* **1986**, *34*, 167–189, doi:10.1016/0022-5096(86)90035-9.
10. Evans, A.G.; Zok, F.W. The physics and mechanics of fibre-reinforced brittle matrix composites. *J. Mater. Sci.* **1994**, *29*, 3857–3896, doi:10.1007/BF00355946.
11. Arai, Y.; Inoue, R.; Goto, K.; Kogo, Y. Carbon fiber reinforced ultra-high temperature ceramic matrix composites: A review. *Ceram. Int.* **2019**, *45*, 14481–14489, doi:10.1016/j.ceramint.2019.05.065.
12. Vinci, A.; Zoli, L.; Sciti, D.; Melandri, C.; Guicciardi, S. Understanding the mechanical properties of novel UHTCMCs through random forest and regression tree analysis. *J. Mater. Des.* **2018**, *145*, 97–107, doi:10.1016/j.matdes.2018.02.061.
13. Sciti, D.; Silvestroni, L. Processing, sintering and oxidation behavior of SiC fibers reinforced ZrB_2 composites. *J. Eur. Ceram. Soc.* **2012**, *32*, 1933–1940, doi:10.1016/j.jeurceramsoc.2011.10.032.
14. Naslain, R. Design, preparation and properties of non-oxide CMCs for application in engines and nuclear reactors: An overview. *Compos. Sci. Technol.* **2004**, *64*, 155–170, doi:10.1016/S0266-3538(03)00230-6.

15. Zhang, Y.; Zuo, T.T.; Tang, Z.; Gao, M.C.; Dahmen, K.A.; Liaw, P.K.; Lu, Z.P. Microstructures and properties of high-entropy alloys. *Prog. Mater. Sci.* **2014**, *61*, 1–93, doi:10.1016/j.pmatsci.2013.10.001.
16. Naslain, R. Materials design and processing of high temperature ceramic matrix composites: State of the art and future trends. *Adv. Compos. Mater.* **1999**, *8*, 3–16, doi:10.1163/156855199X00029.
17. Delhaes, P. Chemical vapor deposition and infiltration processes of carbon materials. *Carbon N. Y.* **2002**, *40*, 641–657.
18. Aoki, T.; Ogasawara, T.; Okubo, Y.; Yoshida, K.; Yano, T. Fabrication and properties of Si−Hf alloy melt-infiltrated Tyranno ZMI fiber/SiC−based matrix composites. *Compos. Part A* **2014**, *66*, 155–162, doi:10.1016/j.compositesa.2014.07.009.
19. Aoki, T.; Ogasawara, T. Tyranno ZMI fiber/$TiSi_2$−Si matrix composites for high-temperature structural applications. *Compos. Part A* **2015**, *76*, 102–109, doi:10.1016/j.compositesa.2015.05.018.
20. Wang, S.; Zhu, Y.; Chen, H.; Li, W.; Chen, Z. Effect of Cu on the ablation properties of C_f/ZrC composites fabricated by infiltrating C_f/C preforms with Zr-Cu alloys. *Ceram. Int.* **2015**, *41*, 5976–5983, doi:10.1016/j.ceramint.2015.01.036.
21. Pi, H.; Fan, S.; Wang, Y. C/SiC−ZrB_2−ZrC composites fabricated by reactive melt infiltration with $ZrSi_2$ alloy. *Ceram. Int.* **2012**, *38*, 6541–6548, doi:10.1016/j.ceramint.2012.05.035.
22. Inoue, R.; Kakisawa, H.; Kagawa, Y. Fracture criterion of short carbon fiber-dispersed SiC matrix composite under mixed mode loading condition. In Proceedings of the 10th Pacific Rim Conference on Ceramic and Glass Technology, San Diego, CA, USA, 2−7 June 2013; p. 53.
23. Inoue, R.; Yang, J.M.; Kakisawa, H.; Kagawa, Y. Mixed-mode fracture criterion of short carbon fiber-dispersed SiC matrix composite. *J. Ceram. Sci. Technol.* **2017**, *8*, 223–232, doi:10.4416/JCST2016-00108.
24. Inoue, R.; Yang, J.M.; Kakisawa, H.; Kagawa, Y. Mode I fracture toughness of short carbon fiber-dispersed SiC matrix composite fabricated by melt infiltration process. *Ceram. Int.* **2013**, *39*, 8341–8346, doi:10.1016/j.ceramint.2013.04.014.
25. Inoue, R.; Arai, Y.; Kubota, Y.; Goto, K.; Kogo, Y. Oxidation behavior of carbon fiber-dispersed ZrB_2−SiC−ZrC triple phase matrix composites in an oxyhydrogen torch environment. *Ceram. Int.* **2018**, *44*, 8387–8396, doi:10.1016/j.ceramint.2018.02.031.
26. Inoue, R.; Arai, Y.; Kubota, Y. Oxidation behaviors of ZrB_2−SiC binary composites above 2000 °C. *Ceram. Int.* **2017**, *43*, 8081–8088, doi:10.1016/j.ceramint.2017.03.129.
27. Inoue, R.; Arai, Y.; Kubota, Y.; Kogo, Y.; Goto, K. Initial oxidation behaviors of ZrB_2−SiC−ZrC ternary composites above 2000 °C. *J. Alloys Compd.* **2018**, *731*, 310–317, doi:10.1016/j.jallcom.2017.10.034.
28. Kubota, Y.; Tanaka, H.; Arai, Y.; Inoue, R.; Kogo, Y.; Goto, K. Oxidation behavior of ZrB_2−SiC−ZrC at 1700 °C. *J. Eur. Ceram. Soc.* **2017**, *37*, 1187–1194, doi:10.1016/j.jeurceramsoc.2016.10.034.
29. Arai, Y.; Inoue, R.; Tanaka, H.; Kogo, Y.; Goto, K. In-situ observation of oxidation behavior in ZrB_2−SiC−ZrC ternary composites up to 1500 °C using high-temperature observation system. *J. Ceram. Soc. Jpn.* **2016**, *124*, 890–897, doi:10.2109/jcersj2.16043.
30. Zou, L.; Wali, N.; Yang, J.-M.; Bansal, N.P. Microstructural development of a C_f/ZrC composite manufactured by reactive melt infiltration. *J. Eur. Ceram. Soc.* **2010**, *30*, 1527–1535, doi:10.1016/j.jeurceramsoc.2009.10.016.
31. Murray, J.L. The Ti-Zr (Titanium-Zirconium) system. *Bull. Alloy Phase Diagr.* **1981**, *2*, 197–201, doi:10.1007/BF02881478.
32. Arai, Y.; Daigo, Y.; Esuke, K.; Ryo, I.; Yasuo, K. Relationship between the microstructures and Young's modulus of three-dimensional networked porous carbon material. *J. Mater. Sci.* **2021**, *56*, 10338–10352, doi:10.1007/s10853-021-05950-x.
33. Inoue, R.; Li, G.; Kojo, E.; Nakajima, M.; Kubota, Y.; Kogo, Y. Experimental investigation and analysis of mechanical properties of three-dimensionally networked porous carbon material. In Proceedings the 12th Pacific Rim Conference on Ceramic and Glass Technology: Ceramic Transactions, Waikoloa, HI, USA, 21−26 May 2018; pp. 77–84.
34. Einset, E.O. Capillary infiltration rates into porous media with applications to silcomp processing. *J. Am. Ceram. Soc.* **1996**, *79*, 333–338, doi:10.1111/j.1151-2916.1996.tb08125.x.
35. Dubrovinskaia, N.A.; Dubrovinsky, L.S.; Saxena, S.K.; Ahuja, R.; Johansson, B. High-pressure study of titanium carbide. *J. Alloys Compd.* **1999**, *289*, 24–27, doi:10.1016/S0925-8388(99)00159-0.
36. Rahimzadeh, E.; Joshi, N.R.; Singh, S. Thermal expansion of ZrC from 120 to 300 K by an X-ray powder method. *J. Am. Ceram. Soc.* **1984**, *67*, C-139–C-140, doi:10.1111/j.1151-2916.1984.tb19623.x.
37. Ivashchenko, V.I.; Turchi, P.E.A.; Shevchenko, V.I. First-principles study of elastic and stability properties of ZrC−ZrN and ZrC-TiC alloys. *J. Phys. Condens. Matter* **2009**, *21*, doi:10.1088/0953-8984/21/39/395503.
38. Li, Y.; Katsui, H.; Goto, T. Phase decomposition of TiC−ZrC solid solution prepared by spark plasma sintering. *Ceram. Int.* **2015**, *41*, 14258–14262, doi:10.1016/j.ceramint.2015.07.055.
39. Chase, M.W., Jr. *NIST-JANAF Thermochemical Tables*, 4th ed.; American Institute of Physics: Woodbury, NY, USA, 1998.